

1 **Ocean—atmosphere—wave characterization of a wind jet**
2 **(Ebro shelf, NW Mediterranean Sea)**

3

4

5

6

7

8

9 **Manel Grifoll¹, Jorge Navarro², Elena Pallares¹, Laura Ràfols^{1,3}, Manuel Espino¹**
10 **and Ana Palomares²**

11

12 [1]{LIM/UPC (BarcelonaTech), Barcelona, Spain}

13 [2]{CIEMAT, Madrid, Spain}

14 [3]{Meteocat, Barcelona, Spain}

15

16 Correspondence to: M. Grifoll (manel.grifoll@upc.edu)

1

2 **Abstract**

3 In this contribution the wind jet dynamics in the northern margin of the Ebro River shelf (NW
4 Mediterranean Sea) are investigated using coupled numerical models. The study area is
5 characterized by persistent and energetic offshore winds during autumn and winter. During
6 these seasons, a seaward wind jet usually develops in a ~50km wide band offshore. The
7 COAWST (Coupled Ocean—Atmosphere—Wave—Sediment Transport) modelling system
8 was implemented in the region with a set of downscaling meshes to obtain high-resolution
9 meteo-oceanographic outputs. Wind, wave and water current were compared with in situ
10 observations and remote-sensing-derived products with an acceptable level of agreement.
11 Focused on an intense offshore wind event, the modelled wind jet appears in a limited area
12 offshore with a strong spatial variability. The wave pattern during the wind jet is
13 characterized by the developing of bimodal directional spectra, and the ocean circulation
14 tends to present well-defined two-layer flow in the shallower region (i.e. inner shelf). The
15 outer shelf tends to be dominated by mesoscale dynamics such as the slope current. Due to the
16 limited fetch length, ocean surface roughness considering sea state (wave-atmosphere
17 coupling) modifies to a small extent the wind and significant wave height under severe cross-
18 shelf wind events. However, the coupling effect in the wind resource assessment may be
19 relevant due to the cubic relation between the wind intensity and power.

20 Keywords: wind jet, COAWST, ocean—atmosphere coupling, wind power assessment

21 **1 Introduction**

22 Coastal areas are often characterized by highly variable and heterogeneous wind, wave and
23 current conditions, which make the numerical prediction of the meteo-oceanographic
24 processes difficult. For instance, wind jets induced by orographic effects present strong spatial
25 wind field variability due to the orographic characteristics (e.g. Shimada and Kawamura,
26 2006; Zhai and Bower, 2013). Due to the persistence in wind intensity and direction, these
27 regions are preferential sites for the installation of offshore wind farms (Nunalee and Basu,
28 2013). In case of coastal regions, the resultant offshore winds decisively influence the
29 exchange of water mass and material along the shelf/slope (Jordà et al., 2005; Barton et al.,
30 2009). Despite the relatively limited fetch in the wind jet region, the wave height can be
31 relevant, interacting with bimodal features (Shimada and Kawamura, 2006). In this sense,

1 several contributions have highlighted the influence of variable wind conditions in relatively
2 small-scale areas (such as wind jet), influencing wind—wave generation (Shimada and
3 Kawamura, 2006; Bolaños et al., 2007; Alomar et al., 2014) or modifying ocean circulation
4 patterns (Csanady, 1980; Zhai and Bower, 2013; Schaeffer et al. 2011; Klaić et al., 2011).

5 In coastal zones the air—sea momentum transfer presents high complexity due to the
6 dependence of wind intensity on sea bottom roughness. The relevance of the atmospheric
7 bottom roughness increasing due to waves has been investigated in recent years (Janssen,
8 1989; Janssen and Viterbo, 1996; Lionello et al.1998; Taylor and Yelland, 2001; Oost et al.,
9 2002; Drennan et al., 2003). In this sense, advanced computational tools allowed the feedback
10 of meteo-oceanographic momentum and heat transfer to be addressed numerically (Warner et
11 al., 2010; Zambon et al., 2014). Warner et al. (2010) developed a fully coupled numerical
12 system (COAWST: Coupled Ocean—Atmosphere—Wave—Sediment Transport) to
13 investigate the impact of storms on coastal systems. Using COAWST, Olabarrieta et al.
14 (2012) and Renault et al. (2012) proved numerically that the wave-induced ocean surface
15 roughness is a key parameter in the air—sea momentum transfer. Under severe storm
16 conditions (hurricanes and cyclones), this parameter influences the spatial and temporal
17 evolution of the meteo-oceanographic variables. Other recent examples that use a fully
18 numerical model to investigate the air—sea interaction and its effect on oceanographic
19 processes are found in Nelson and He (2012) and Drews (2013).

20 The case of the Ebro River shelf (NW Mediterranean Sea; see Figure 1) is characterized by
21 strong, dry and usually cold wind that blows from the north-west through the Ebro valley. The
22 westerly wind, greatly affected by the orography, is channelized into a limited band, forming
23 a wind jet (Jansà, 1985; Spanish Ministry of Energy, 2004). The synoptic situation is related
24 to an anticyclone in the Bay of Biscay and a low-pressure area in the Mediterranean Sea
25 (Riosalido et al., 1986; Font, 1990; Martín-Vide, 2005; Cerralbo et al., 2015). Offshore wind
26 is more usual and intense during autumn and winter, when larger atmospheric pressure
27 gradients take place and cause stronger winds with advection of cold air, but a small
28 atmospheric pressure difference along the Ebro valley is sufficient to initiate wind during any
29 season (Riosalido et al., 1986; Cerralbo et al., 2015).

30 The objective of this contribution is to describe the meteo-oceanographic processes associated
31 with a wind jet developing at the northern margin of the Ebro River shelf. This work provides
32 insight into wind jet in an orographically complex region, such as the Ebro delta shelf,

1 describing the main wind, wave and current patterns and the feedback relative to the air—sea
2 momentum transfer in terms of wave-induced ocean surface roughness. After the introduction
3 (Section 1), in Section 2 (Methods) we describe the study area, the COAWST model
4 implementation and the wind jet event selected to investigate in detail the meteo-
5 oceanographic dynamics. Then, in Results (Section 3) we show the most relevant meteo-
6 oceanographic processes observed and a detailed skill assessment of the fields modelled,
7 comparing them with a set of available data (i.e. in situ observations and remote-sensing
8 products). Also, the feedback in the air—sea momentum transfer in terms of wave-induced
9 ocean surface roughness is investigated with a set of coupled simulations testing different
10 air—sea momentum transfer formulations. Afterwards, we discuss (Section 4) the relevance
11 and particularities of the dynamics of the wind jet area in terms of waves, winds and currents,
12 comparing with previous investigations. The implications of the wind—wave coupling in
13 terms of the wind resource assessment are highlighted. We close with the conclusions
14 (Section 5).

15 **2 Methods**

16 **2.1 Study area and observations**

17 The meteorological patterns over the NW Mediterranean Sea exhibit sharp gradients
18 associated with the topographic control on synoptic fluxes (Jansà, 1985; Martin-Vide and
19 Olcina, 2001). Regional wind analysis reveals strong and persistent cross-shelf winds. A
20 channelization effect associated with the Ebro valley triggers north-westerly winds (called
21 “Mestral”), resulting in a wind jet. Previous studies based on long-term wind measurements in
22 the proximity of the region showed that winds have a persistent seasonal pattern (Font, 1990;
23 Cerralbo et al., 2015; Grifoll et al., 2015). During winter and autumn, a dominant north-
24 westerly component caused by wind channelization was observed. For instance, recent wind
25 measurements revealed that cross-shelf winds were observed more than 60 % of the time
26 during these seasons (Grifoll et al., 2015). In this period, the energy is concentrated in the low
27 frequencies associated with synoptic scales (periods of 2—5 days, corresponding with the
28 passage of weather systems). However, the warmer period (spring and summer) is
29 characterized by high variability with a dominance of south-westerly winds. This means that
30 during spring and summer the relative contribution of the daily components (breezes) to the

1 variability increases with respect to the synoptic winds (Font, 1990; Cerralbo et al., 2015).
2 The warmer seasons are less energetic than the cold seasons in terms of wind intensity.
3 The Ebro River delta is located immediately to the south of the wind jet region, and the
4 average annual river discharge ranges between 300 and 600m³·s⁻¹. The curvature of the bay
5 partially shelters it from southerly waves. Regional wave climate in this area is characterized
6 by south-east and east sectors, the latter being the most energetic due to the largest fetches
7 (Bolaños et al., 2007).

8 Oceanographic investigations in the Ebro River region were focused primarily on the outer
9 shelf and slope dynamics of the southern margin (Font, 1990; Palanques et al., 2002; Salat et
10 al., 2002; Jordà, 2005) with relevant eddy activity (Redondo et al., 2013). The circulation in
11 these regions is dominated by the inertial band, with a relevant signal of the slope current
12 associated at the regional Northern Current (Jordà, 2005). Observational analyses have
13 revealed that the inner and mid-shelf (less than 50m water depth) dynamics in the Ebro shelf
14 are characterized by a strong influence of the frictional component of the flow (Jordà, 2005,
15 Grifoll et., 2015). Furthermore, the regional response to wind jets is not clear due to the
16 complex bathymetry and the spatial variability of the wind jet. Durand et al. (2002) and
17 Mestres et al. (2003) showed that the effects of the salinity river plume are important only
18 near the river mouth (order of 10km offshore from the river mouth).

19 As a part of large effort to collect physical data and implement numerical tools for the
20 assessment of offshore wind energy potential, a buoy was moored in the northern margin of
21 the Ebro shelf where the wind jet develops (see Figure 1). The buoy was moored 3.1km from
22 the coast at 43.5m bottom depth, measuring wind, waves and water currents for one year. A
23 TRIAXYS directional wave sensor mounted on the moored buoy was used to record
24 statistical wave spectra parameters. Wind speed and direction were measured at 4m height
25 every 10min using an ultrasonic wind sensor (Gill Instruments) for one year (November 2011
26 to November 2012). Water currents were measured with a SonTek acoustic Doppler
27 currentmeter profiler (ADCP) at 500kHz every hour using 20 vertical layers (layer depth was
28 2m). The mooring period covered more than one year (from November 2011 to December
29 2012).

30 Additionally, satellite-measured winds were used for the numerical model validation. Sea
31 wind intensity and direction were obtained from the National Climatic Data Center (NCDC-
32 NOAA, <http://www.ncdc.noaa.gov/oa/rsad/air-sea/seawinds.html>). This product is the result

1 of a spatial and temporal interpolation of the data received from the different satellites passing
2 through the study area during a time interval, and it has 6h time resolution and 0.25° spatial
3 resolution.

4 **2.2 Numerical model and meshes**

5 The COAWST modelling system (Warner et al., 2010) was used in this study. COAWST
6 relies on the 3-D ocean modelling ROMS (Regional Ocean Modeling System; see Haidvogel
7 et al., 2000), the phase-averaged wave model SWAN (Simulating WAaves Nearshore; see
8 Booij et al., 1999), the non-hydrostatic meteorological model WRF (Weather Research and
9 Forecasting; Skamarock et al., 2005) and the sediment transport module CSTMS (Community
10 Sediment Transport Modeling System; Warner et al., 2008). The ocean model ROMS is a
11 free-surface, terrain-following numerical model which resolves the three-dimensional
12 Reynolds-averaged Navier—Stokes (RANS) equations using hydrostatic and Boussinesq
13 approximation. The WRF model (Advanced Research WRF version) is a non-hydrostatic,
14 quasi-compressible atmospheric model with a variety of physical parameterizations of sub-
15 grid scale processes for predicting meso- and microscales of motion. The SWAN model
16 solves the wave action balance equation simulating wind generation and propagation in deep
17 and coastal waters. The modelling system COAWST includes the coupler Model Coupling
18 Toolkit (MCT; Jacob et al., 2005) for the transmission and transformation of the physical
19 variables using a parallel computing approach. The COAWST system also allows for the
20 exchange of data fields on different grids using the Spherical Remapping Interpolation
21 Package (SCRIP; Jones, 1998) to compute the interpolation weights.

22 The largest wave domain (mesh O1) covers the western Mediterranean Sea, which is
23 considered large enough to capture the wave generation in the study area. The SWAN model
24 implementation used amends the underestimation in the wave growth rates reported by
25 Alomar et al. (2014) and Rogers et al. (2003) in a low- and medium-frequency energy
26 spectrum. The measure adopted was introduced by Pallares et al. (2014) and consists in
27 modifying the whitecapping dissipation term (see Appendix 1).

28 The largest water circulation domain (mesh O3) is nested into the daily MyOcean-MEDSEA
29 product (Tonani et al., 2009), with a horizontal resolution of 1/16°x1/16° and 72 unevenly
30 spaced vertical levels, in order to provide suitable boundary conditions for the oceanographic
31 variables in terms of water velocity, sea level, temperature and salinity. The 3D ocean model

1 implementation (ROMS) includes a generic length scale turbulent mixing scheme (Umlauf
2 and Burchard, 2003), with coefficients selected to parameterize the K-epsilon scheme (Rodi,
3 1987) and fourth-order biharmonic Laplacian viscosity and mixing terms on geopotential
4 surfaces for velocity and tracers, respectively, both with constant coefficients of $0.5\text{m}^4\text{s}^{-2}$. The
5 bottom boundary layer was parameterized using a log profile with bottom roughness equal to
6 0.005m. The time-interval for data exchange between the models is 600s.

7 The atmospheric model is nested into the ECMWF ERA-Interim reanalysis product
8 considering four downscaling meshes – M1, M2, M3 and M4 with resolutions of 27km, 9km,
9 3km and 1km, respectively – to obtain suitable grid resolution for the complex orography of
10 the region (see Figure 1). The WRF implementation uses a Mellor—Yamada—Nakanishi—
11 Niino (MYNN) level 2.5 planetary boundary layer scheme. The nesting strategy consists of a
12 set of different downscaling meshes (Figure 1c and Table 1). The ocean—atmospheric—wave
13 online coupling was implemented in the finer domain (mesh O4 for the wave and circulation
14 model, and mesh M4 for the meteorological model) where the scale of the coupling process
15 due to cross-shelf winds may be more evident in the results. In this case, air—sea coupled
16 effects are included considering Taylor and Yelland formulation (Taylor and Yelland, 2001),
17 for the ocean surface roughness modification due to the wave effect, and vortex force for the
18 wave effects on currents (Olabarrieta et al., 2012).

19 **2.3 Episode description and numerical sensitivity test**

20 As we noted in the introduction, the air—sea momentum transfer presents high complexity
21 due to the relation of wave characteristics and the sea bottom roughness, which in turns affect
22 the wind field. In order to investigate the air—sea momentum transfer in the wind jet, a set of
23 simulations have been designed applying different air—sea momentum transfer formulations
24 included in the COAWST modelling system. The sensitivity tests pursue an evaluation of the
25 “coupling” effects on two principal variables involved in the air—sea momentum transfer:
26 wind intensity (W) and significant wave height (H_s). In this sense three different formulations
27 have been tested (see Appendix 2), which consider the modification of the atmospheric
28 bottom roughness due to the waves. In consequence, we compare directly the “coupled”
29 results with an “uncoupled” simulation where the bottom roughness length is only a function
30 of the wind stress. The sensitivity tests are as follows: CHK for the simulation considering the
31 bottom roughness as a function of the wind stress (uncoupled with the wave sea state) using
32 the Charnock coefficient equal to 0.016, T—Y simulation considering the Taylor and Yelland

1 formulation (Taylor and Yelland, 2001), DRE using the Drennan formulation proposed by
2 Drennan et al. (2003) and OOST simulation considering the formulation introduced by Oost
3 et al. (2002). Two numerical points are chosen to compare the results for the sensitivity test
4 simulations. One point is near the buoy's moored position (where the numerical results are
5 also compared with the measurements). The second point is located 30km offshore of the
6 measurement point (see control point in Figure 1). This point has been chosen in order to
7 capture the wave growth due to cross-shelf winds and evaluate properly the coupling—
8 uncoupling differences.

9 We select a cross-shelf wind event in order to characterize in detail the meteo-oceanographic
10 dynamics of the wind jet. The episode selected for the sensitivity tests lasted from the 19th of
11 March 2012 to the 23rd of March 2012. The synoptic situation during the selected episode
12 corresponds to a typical offshore wind event induced by atmospheric pressure differences (see
13 Figure 2). A high-atmospheric-pressure area is centred over the North Atlantic Ocean, with
14 the anticyclonic edge affecting part of the Iberian Peninsula. The low pressure is located in
15 the centre of Europe. In this situation the cross-shore winds in the Ebro delta zone are
16 intensified. The sequence of wind field modelled in the Catalan coast mesh during the wind
17 jet period is characterized by a rise of wind intensity during the 20th and 21st of May, leading
18 to a wind jet in the northern margin of the Ebro delta (see daily-averaged wind intensity in
19 Figure 3). Then, the cross-shore winds remain strong during the 22nd of May, decreasing
20 during the 23rd of May 2012.

21 **3 Results**

22 **3.1 Description of meteo-oceanographic processes and skill assessment**

23 The skill assessment of the model is carried out for different meshes in function the spatial
24 domain of the observations. Modelled winds during the simulation period reproduce the main
25 wind directions previously reported in the study area. Offshore wind prevails throughout the
26 year, intercalated with southerly winds during spring and summer (i.e. sea breeze). The
27 adjustment of the wind time series into a Weibull distribution is used to evaluate the statistical
28 inter-comparison between wind observations (measured from the buoy and satellite) and the
29 3km WRF model results (mesh M3). Blended Sea Winds were used from the NCDC-NOAS
30 SeaWinds project which contain 6-hourly globally gridded, high-resolution ocean surface
31 vector winds and wind stresses on a global 0.25° grid. Figure 4 shows the Weibull

1 distributions considering the wind intensity time series. Also the global model (i.e. ECMWF)
2 used for WRF model downscaling is included. The results show that for high and medium
3 range wind speeds (> 2.5 m/s) the numerical simulation presents better agreement with the
4 wind measurements than the global model and the gridded satellite wind estimations.
5 Although the global wind model assimilates the satellite information, the Weibull distribution
6 of the high-resolution model presents a better level of agreement with the observations. A
7 snapshot of the SeaWinds product was compared with the numerical outputs in Figure 5.
8 Wind patterns from both products present a significant level of agreement in both components
9 assuming the coarser resolution of the SeaWinds. Additional verification is presented in Table
10 2 using model—observation statistics in terms of wind intensity for the whole year of 2012.
11 Correlation coefficient (R) is almost 0.8 and the root mean square error (RMSE) and the Bias
12 are smaller than the mean and the standard deviation obtained from the observations. In
13 summary, modelled winds show an acceptable level of agreement with the observations.

14 In Figure 6, time series comparing the results obtained from the coupled SWAN model (mesh
15 O3) and the buoy measurements (see position in Figure 1) are shown. The time series
16 comparison corresponds to the significant wave height (H_s), the mean wave period (T_{m01}) and
17 the mean wave direction (θ_w). Table 2 presents the error statistics for the whole year for mesh
18 O3 in terms of H_s and T_{m01} . In general, the model reproduces the observed values in terms of
19 mean behaviour and variability. Error statistics are similar with previous numerical
20 investigations in the region; Pallares et al., (2014) obtained values of R ranges 0.68 to 0.91 for
21 H_s .

22 Figure 7.right show a snapshot of the waves' directional spectra during the wind jet period
23 selected at the measuring point; the results reveal the tendency to develop bimodal directional
24 spectra due to the co-existence of sea and swell waves. Directional spectra presents a peak
25 around 315° mean wave direction associated with the growing wave due to the wind jet and
26 another peak around 135° associated with the swell. Despite the limited fetch, larger wave
27 frequencies (smaller wave period) are obtained for the 315° wave direction peak than for the
28 135° wave direction peak. In Figure 7.left the directional spectra for a period without wind jet
29 are also shown for comparison. In this case, unimodal wave spectra is obtained. In summary,
30 the high-resolution mesh (O4) is able to capture the bimodal spectra during wind jet.
31 Unfortunately, only the statistical spectra parameters were recorded in the buoy
32 measurements, and full spectra comparison is not possible.

1 The water circulation observed at the buoy is characterized by an alignment of the flow
2 following the isobaths. The principal component analysis of the flow for the observed depth-
3 averaged currents reveals an angle similar to the coastline orientation ($\sim 26^\circ$). As the cross-
4 shelf flow is limited by the coastline, the variability in this direction is smaller than in along-
5 shelf direction: standard deviation is $2.3\text{cm}\cdot\text{s}^{-1}$ in cross-shelf direction versus $7.4\text{cm}\cdot\text{s}^{-1}$ in
6 along-shelf direction. However, the water circulation during the wind jet events shows a
7 different pattern. During these events, the cross-shelf flow variability increases ($3.8\text{cm}\cdot\text{s}^{-1}$ for
8 the wind jet event selected), with either two-layer flow or an offshore flow in the whole water
9 column. As an example of water current response during wind jet event, the along-shelf and
10 cross-shelf velocities are shown in Figure 8 for May 2012 at the observational point (negative
11 values mean south-westward/onshore and positive north-eastward/offshore). The surface
12 currents in the cross-shelf direction intensify, causing an eventual two-layer flow during the
13 peak of the wind intensity (21st of May). When the wind jet calms down, the cross-shelf
14 velocities are small while the along-shelf flow intensity is larger than that of the cross-shelf.
15 The along-shelf current observed during wind jet events tends to reverse from south-westward
16 to north-eastward.

17 The skill assessment of the numerical results in terms of current (water velocity) was carried
18 out following a similar scheme to the one used for winds and waves. The numerical model
19 validation with ADCP observations shows an acceptable level of agreement according to the
20 comparison for the wind jet event. For instance, Figure 8 shows a noticeable agreement
21 between the observed and modelled currents in the water column for both along- and cross-
22 shelf components. In addition, Table 2 presents the error statistics for the depth-averaged
23 velocity measurements compared with the numerical model results for the wind jet event.
24 Skill assessment is better in depth-averaged along-shelf flow in comparison to cross-shelf
25 (e.g. R equal 0.82 to vs. 0.24) due to the frequent two-layer flow structure observed in cross-
26 shelf measurements during wind-jet events giving rise a weak depth-averaged cross-shelf
27 velocity.

28 The spatial water circulation modelled during the wind jet event (21st of May) is shown in
29 Figure 9 for two different depths: sub-surface (2m water depth) and intermediate (50m water
30 depth) for O3 mesh. Depth-averaged velocities are also presented in Figure 9. The surface
31 current modelled at 1km (mesh O3) and 250m (mesh O4) grid resolution presents a relatively
32 homogeneous offshore direction qualitatively that is well correlated with the spatial

1 distribution of the wind intensity. In this case, the surface current is seldom affected by the
2 topographic features such as the Ebro delta. Consistent with Figure 8, at deeper layers the
3 flow direction turns onshore, resulting in a two-layer flow in which the current intensity is
4 lower than that of the surface layer (Figure 9, centre). The depth-averaged flow is small due to
5 the balance between the sheared two-layer flow; however, a flow component slightly appears
6 that is aligned with the isobaths in the deeper areas of the continental shelf. Related to that, a
7 clear signal of the slope current is observed in the results at -50m and depth-averaged
8 currents.

9 **3.2 Ocean surface roughness numerical experiments**

10 The wind intensity and the significant wave height during the selected wind jet event for the
11 four simulations are shown in Figure 10 (for the control and observational points shown in
12 Figure 1). Comparing the numerical results and the observations (Figure 10, upper sub-plots),
13 all the numerical simulations reproduces the wind intensity and the significant wave height
14 with a similar level of agreement. The uncoupled (CHK) and coupled simulations (e.g. T-Y,
15 OOST and DRE) only present differences in the numerical outputs during the joint occurrence
16 of strong winds and wave peaks in the control point. Waves and wind intensity numerical
17 results at the observational point do not presents significant changes among the four
18 simulations due to the limited fetch conditions which means lower significant wave height in
19 comparison to control point. During the calm period (at beginning and end of the wind jet
20 event) the differences among the four simulations are not appreciable. Numerical coupled
21 results does not present better agreement at the observational point than the uncoupled mode
22 results. Comparing the error statistics for the observational point among the three coupled
23 numerical simulations we cannot assure which formulation ensures a better skill assessment
24 (Table 3). At control point the magnitude of the wind intensity and the significant wave height
25 is larger for the uncoupled simulation (CHK) in comparison to coupled simulations (Figure
26 10, bottom sub-plots). Maximum differences of $3 \text{ m}\cdot\text{s}^{-1}$ in wind intensity and 0.3 m in
27 significant wave height are obtained if we compare OOST and CHK simulations. In
28 consequence, small differences are found between coupled and uncoupled simulations when
29 wave conditions increases.

1 4 Discussion

2 The shape of the wind jet modelled is benefited by the high resolution meshes used in our
3 investigation. According to our results, the wind jet approximately covers an area of 50 km
4 width offshore. This area is in agreement with the wind intensity atlas provided by the
5 Spanish Ministry of Energy (see Figure 11) obtained from a long-term reanalysis product (15
6 years using the MASS model). In this sense, high-resolution meshes used in this
7 investigations (i.e. 1 km and 3 km grid resolution) are suitable for an accurate wind jet
8 modelling. As it was pointed out by Alomar et al. (2014) and Cerralbo et al. (2015), the
9 relevance of winds in the ocean response in terms of waves and currents justifies the high-
10 resolution in the modelling investigations in Ebro Delta region.

11 Our results have shown an acceptable representation of the bimodal structure of the
12 significant wave height and support the conclusions highlighted by Alomar et al (2014), who
13 note that a high spatial resolution of wind field is required to represent acceptable numerical
14 wave field in a very limited fetch conditions. The occurrence of bimodal wave features may
15 also have different implications: the first one is that, because of the spatial resolution, the
16 local northwesterly wind that produced the second peak of spectra may not have been
17 detected in previous investigations (Bolaños et al., 2005, 2006; Sánchez-Arcilla et al., 2008;
18 Alomar et al., 2014). The second implication is related to the momentum transfer: several
19 authors have highlighted that under mixed wave-train conditions the ocean surface roughness
20 may increase appreciably (Sánchez-Arcilla et al., 2008). Also, the wave modelling deserves a
21 particular comment related to the good fitting of wave results in comparison to previous
22 investigations (Bolaños et al., 2007; Sánchez-Arcilla et al., 2008). Statistical errors were
23 reduced significantly due to the young sea developed in the wind jet region likely thanks to
24 the modification of a parameter relative to whitecapping dissipation (Pallares et al., 2014). In
25 particular, smaller root mean square errors were obtained in the mean wave period variable,
26 which presented a large uncertainty (Bolaños et al., 2007; Sánchez-Arcilla et al., 2008;
27 Alomar et al., 2014).

28 As we noted in the Results section, the water circulation pattern showed differential behaviour
29 for the long-term water circulation in comparison to the wind jet event. For the long-term
30 circulation and in the shallow region, the frictional response prevails, with the along-shelf
31 flow variability being larger than the cross-shelf flow, similar to other investigations in the
32 inner and mid-shelf (see review in Lentz and Fewings, 2012). However, a different picture

1 occurs during the wind jet event. In this case a characteristic surface current is high correlated
2 to the offshore wind. According to the numerical outputs and in situ observations shown in
3 Figure 8, a deeper onshore flow, opposing the surface layer flow offshore, is developed. This
4 flow is relatively weak due to the prevalence of the along-shelf component which increases
5 offshore. These circulation patterns are consistent with other investigations (e.g. Horwitz and
6 Lentz, 2014; Fewings et al., 2008; Dzwonkowski et al., 2011) where a well-developed two-
7 layer flow due to intense cross-shelf winds tends to occur when the turbulent layers overlap
8 (water depth in the inner shelf is of the order of metres to tens of metres according to Lentz
9 and Fewings, 2012). In the mid- and outer shelf, the flow tends to be oriented in the along-
10 shelf direction due to the prevalence of the regional response to the wind jet and the slope
11 current. In this sense, the frictional adjustment time due to the wind (inversely proportional to
12 the depth) varies in the continental shelf section and may be of the order of days in the mid-
13 /outer shelf (Csanady, 1982). As a consequence, the expected response at deeper layers will
14 also be dependent on processes acting at larger scales than wind jet (i.e., baroclinic forcing,
15 mesoscale activity etc.) such as the slope current signal observed at 50m water depth and
16 depth-averaged currents in the numerical results (Figure 9). The along-shelf flow in the inner
17 shelf is presumably influenced by the regional response to the wind jet at the stratification in
18 the water column and the barotropic pressure gradient adjustment due the spatial wind
19 variability. These factors play an important role in the resultant water circulation pattern and
20 its variability deserves additional numerical efforts and extended local wind and sea level
21 information. For instance, Oey et al. (2004) and Liu and Weisberg (2012) include extended
22 measurements to investigate the water circulation' response to spatial wind and the particular
23 role of the barotropic pressure gradients. Finally, it is worth noting that the interaction
24 between offshore winds and regional circulation was filtered in previous investigations in the
25 region (Font, 1990; Salat et al., 2002; Jordà, 2005).

26 Several investigations have found the importance of the sea state in the impact on the air—sea
27 momentum flux; in particular the calculations based on the Charnock constant underestimated
28 the air—sea momentum transfer (e.g. Janssen and Viterbo, 1996; Drennan et al., 2003) which
29 can be significant under mixed seas (Sanchez-Arcilla et al., 2008). In the northern margin of
30 the Ebro delta and during the wind jet, no relevant differences were found when comparing
31 the significant wave period and the wind intensity between numerical model and observations
32 for the observational point. During calm periods, the averaged conditions prevail over
33 energetic events, so the feedback of the air—sea momentum does not show significant

1 differences. The detailed analysis of the 21st -22nd of May event showed significant
2 differences between the coupled and uncoupled cases for significant wave height and wind
3 intensity offshore of the wind jet (e.g. control “offshore” point). When we compare the
4 coupling numerical results (i.e. T—Y, OOST and DRE) versus CHK results, we observe that
5 the wind intensity at the control point is affected significantly by the sea state during the
6 energetic event. For the coupling simulations the wind intensity is reduced due to the
7 increasing wave-induced ocean surface roughness. This behaviour is consistent with other
8 coupling atmosphere—ocean investigations under a high level of meteorological energy (e.g.
9 Olabarrieta et al., 2012). In parallel, the wave field is modified by the feedback between wave
10 and wind stress. During the energetic wind event selected, H_s is lower in comparison to the
11 uncoupled case (CHK), consistent with other numerical experiments (Webber, 1993; Warner
12 et al., 2010; Olabarrieta et al., 2012) and observational investigations (Yelland et al. 1998;
13 Edson, 2008) which found that the momentum flux is underestimated using the Charnock
14 constant parameter. Unfortunately, the lack of measurements offshore of the observational
15 point (i.e. larger fetch in comparison to observational point) has not allowed to investigate if
16 the coupling simulations present better skill assessment than the uncoupled case.

17 Differences in the primitive variables between the coupled and uncoupled simulations during
18 particular energetic events are relatively small in terms of wind intensity and significant wave
19 height. Furthermore, the assessment of the wind energy resource is relevant in this region with
20 a high potential for wind farm installation due to the large and persistent wind intensity and
21 the relatively large spatial extension of the continental shelf. A simple way to estimate turbine
22 power from wind intensity is based on the idealized machine of blade diameter (D) being
23 equal to 100m (Manwell et al., 2011):

$$P = \rho (2/3D)^2 W^3 \quad (1)$$

24 Wind intensity (W) simulations are taken at 10m height, so a log-law-based conversion is
25 used to obtain wind values at 80m (typical value of turbine hubs). With the converted values
26 of the numerical simulations, we estimate the idealized wind power for the period 21st–22nd
27 of May 2012 at the control point. The power using the CHK wind value is 8.087kW (average
28 wind speed of 11.41m/s); in contrast, using OOST formulations leads to a power of 7.207 kW
29 (average wind speed of 10.98m/s). Intermediate values are obtained for T—Y and DREN
30 formulations: 7.365kW and 7.346kW, respectively. The cubic relationship between wind
31 power and wind velocity highlights the importance of accurate estimations of wind intensity

1 for wind energy resources using coupling techniques (a maximum percentage of 10% is
2 assessed). This example shows the relevance of coupled effects for an accurate wind power
3 assessment for wind farm project plans.

4 The wave-limited fetches and the persistent offshore winds represent particular ocean—
5 atmosphere conditions never investigated before from a full-coupling perspective; only
6 energetic cyclogenesis activity and extreme conditions has been recently modelled and
7 investigated (e.g. Warner et al., 2010, Olabarrieta et al., 2012; Renault et al., 2012; Zambon et
8 al., 2014; Ricchi et al., 2016) where also the heat transfer plays a relevant role in the air—sea
9 coupling. In the mentioned cases, extreme modelled waves and wind benefitted from the use
10 of full-coupling systems. Our case only presents comparable energetic conditions during a
11 very short period of time; however the cubic relationship between the potential wind energy
12 and the wind intensity may justify for engineering purposes the use of coupled formulations
13 between wind and waves. Further observational campaigns and the future use of high-
14 resolution remote-sensing products (e.g. Sentinel-1 and Sentinel-3; Torres et al., 2012 and
15 Malenovsky et al., 2012) will benefit the numerical results and extended physical
16 investigations in such a complex process as wind jet, in particular the role of the air—sea
17 transfer formulations. Our results are also relevant in that they may be useful for further
18 physical investigations in similar domains where the wind jets control the ocean—atmosphere
19 dynamics (Jiang et al., 2009; Barton et al., 2009; Shimada and Kawamura, 2006).

20 **5 Conclusions**

21 Wind jet events, investigated using numerical modelling and both in situ and remote-sensing
22 data, present particular conditions in meteo-oceanographic variables in the northern margin of
23 the Ebro delta. A fully coupled meteo-oceanographic numerical model was implemented,
24 with a good level of agreement in terms of waves, currents and wind fields measured. The
25 numerical results reveal a spatially varying wind pattern, forming a well-limited wind jet. The
26 water current velocity pattern during wind jet is well correlated with the wind intensities in
27 the surface layer. However, in deep layers the flow becomes complex, and other processes of
28 larger temporal and spatial characteristic scales affect the water circulation. The wave
29 modelling during the wind jet events is characterized by the developing of bimodal wave
30 spectra: local wave generation due to wind jet and waves propagated from the open sea.
31 Numerical results from sensitivity tests have shown the relatively small relevance of air—sea
32 transfer formulations considering the significant wave height for the sea bottom roughness

1 estimation. Furthermore, the accurate estimation of the wind energy resource may be
2 benefitted by the coupled numerical modelling. The characteristics of the meteo-ocean
3 variables during the wind jet in the northern Ebro delta may be useful for understanding
4 processes in similar domains under severe cross-shelf wind conditions.

5

1 **Appendix 1. Modification of the whitecapping term in SWAN**

2 Pallarès et al. (2014) performed numerical experiments that aimed to improve the numerical
3 wave predictions in semi-enclosed bays, modifying the dissipation terms in the wave energy
4 balance equation. For this purpose two whitecapping formulations are considered in SWAN,
5 obtained from the pulse-based model of Hasselmann (1974) reformulated in terms of wave
6 number (the WAMDI group, 1988):

7
$$S_{dissw}(\sigma, \theta) = -\Gamma \bar{\sigma} \frac{\bar{k}}{k} E(\sigma, \theta)$$
 , (A1.1)

8 where $\bar{\sigma}$ and \bar{k} denote the mean frequency and the mean wave number, respectively, and the
9 coefficient Γ depends on the wave steepness (Janssen, 1991):

10
$$\Gamma = C_{ds} \left((1 - \delta) + \delta \frac{\bar{k}}{k} \right) \left(\frac{\bar{\sigma}}{\sigma_{PM}} \right)^p$$
 . (A1.2)

11 The coefficients C_{ds} , δ and p can be adapted to the study case; $\bar{\sigma}$ is the overall wave steepness;
12 and σ_{PM} is the value of $\bar{\sigma}$ for the Pierson—Moskowitz spectrum.

13 In SWAN the previously mentioned coefficients are obtained by adjusting the energy balance
14 for idealized wave growth conditions (fully developed wind seas in deep water), despite the
15 wave growth in semi-enclosed domains with highly variable wind fields differing
16 considerably from those idealized conditions. As a result of a calibration process in the NW
17 Mediterranean Sea, which led to a reduction of the wave forecast errors mainly present in the
18 wave period, the coefficients selected for the wind jet region were $\delta=1$, $C_{ds} = 2.36 \times 10^{-5}$ and
19 $p=4$, achieving a notable fit between numerical outputs and wave observations.

20 **Appendix 2. Air—sea momentum transfer formulations (bottom roughness length)**

21 The standard bottom roughness length scale is expressed as a function of the Charnock
22 coefficient (C_a ; typical value of 0.016) and surface wind stress (u_s):

23
$$z_0 = C_a \cdot u_s^2 / g$$
 , (A2.1)

1 where g is the gravity. Coupling online simulations in COAWST allows three different
2 formulations to be chosen to parameterize the bottom roughness considering the wave effects.
3 The formulation of Taylor and Yelland (2001) considers the wave effects:

$$4 \quad z_0 = 1200 \cdot (H_s/L_p)^{4.5} \quad , \quad (A2.2)$$

5 where H_s is the significant wave height and L_p is the wavelength at the peak of the wave
6 spectrum. Drennan et al. (2003) proposed a formulation to estimate z_0 as a function of the
7 phase-wave speed (C_p) and wind friction velocity (u^*):

$$8 \quad z_0 = 3.35 \cdot (u^*/C_p)^{3.4} \quad . \quad (A2.3)$$

9 Similar to Drennan's formulation, Oost et al. (2002) proposed the following formulation based
10 on an experimental data set:

$$11 \quad z_0/L_p = 25.0/\pi \cdot (u^*/C_p)^{4.5} \quad . \quad (A2.4)$$

12 Conceptual differences arise from these formulations: Taylor and Yelland (2001) considers
13 the wave steepness, Drennan et al. (2003) is based on the wave age and Oost et al. (2002)
14 considers effects of both wave steepness and wave age.

15 **Acknowledgements**

16 The authors are thankful to Joan Puigdefàbregas (LIM/UPC, Barcelona), Joaquim Sospedra
17 (LIM/UPC, Barcelona) and Jordi Cateura (LIM/UPC, Barcelona) for the data acquisition. The
18 research leading to these results and data acquisition received funding from Mestral (CTM-
19 2011-30489), Neptune (KIC project 006-2012-R01-IREC-OFF-AERO), Hareamar/Dardo
20 (ENE2012-38772-C02-02), Rises-AM (GA603396), iCOAST project
21 (ECHO/SUB/2013/661009) and MINECO and FEDER who Plan-Wave (CTM2013-45141-
22 R).

23

1 **References**

- 2 Alomar, M., A., Sánchez-Arcilla, R. Bolaños, and A. Sairouni (2014), Wave growth and
3 forecasting in variable, semi-enclosed domains, *Cont. Shelf Res.*, 87, 28–40,
4 doi:10.1016/j.csr.2014.05.008.
- 5 Barton, E. D., M. F. Lavín, and A. Trasviña (2009), Coastal circulation and hydrography in
6 the Gulf of Tehuantepec, Mexico, during winter, *Cont. Shelf Res.*, 29(2), 485–500,
7 doi:10.1016/j.csr.2008.12.003.
- 8 Bolaños-Sanchez, R., A. Sanchez-Arcilla, and J. Cateura (2007), Evaluation of two
9 atmospheric models for wind–wave modelling in the NW Mediterranean, *J. Mar. Syst.*,
10 65(1-4), 336–353, doi:10.1016/j.jmarsys.2005.09.014.
- 11 Booij, N., R. C. Ris, and L. H. Holthuijsen (1999), A third-generation wave model for coastal
12 regions: 1. Model description and validation, *J. Geophys. Res.*, 104(C4), 7649,
13 doi:10.1029/98JC02622.
- 14 Cerralbo, P., M. Grifoll, J. Moré, M. Bravo, A. Sairouni Afif, and M. Espino (2015), Wind
15 variability in a coastal area (Alfacs Bay, Ebro River delta), *Adv. Sci. Res.*, 12, 11–21,
16 doi:10.5194/asr-12-11-2015.
- 17 Csanady, G. T. (1980), Longshore pressure gradients caused by offshore wind, *J. Geophys.*
18 *Res.*, 85(C2), 1076, doi:10.1029/JC085iC02p01076.
- 19 Csanady, G. T. (1982), Circulation in the coastal ocean, *Adva. Geophys.*, 23, 101-183.
- 20 Drennan, W. M., H. C. Graber, D. Hauser, and C. Quentin (2003), On the wave age
21 dependence of wind stress over pure wind seas, *J. Geophys. Res.*, 108(C3), 8062,
22 doi:10.1029/2000JC000715.
- 23 Drews, C. (2013), Using wind setdown and storm surge on Lake Erie to calibrate the air-sea
24 drag coefficient., *PLoS One*, 8(8), e72510, doi:10.1371/journal.pone.0072510.
- 25 Durand, N., A. Fiandrino, P. Fraunié, S. Ouillon, P. Forget, and J. J. Naudin (2002),
26 Suspended matter dispersion in the Ebro ROFI: an integrated approach, *Cont. Shelf Res.*,
27 22(2), 267–284, doi:10.1016/S0278-4343(01)00057-7.
- 28 Dzwonkowski, B., K. Park, and L. Jiang (2011), Subtidal across-shelf velocity structure and
29 surface transport effectiveness on the Alabama shelf of the northeastern Gulf of Mexico,
30 *J. Geophys. Res.*, 116(C10), C10012, doi:10.1029/2011JC007188.
- 31 Fewings, M., S. J. Lentz, and J. Fredericks (2008), Observations of Cross-Shelf Flow Driven
32 by Cross-Shelf Winds on the Inner Continental Shelf, *J. Phys. Oceanogr.*, 38(11), 2358–
33 2378, doi:10.1175/2008JPO3990.1.
- 34 Font, J. (1990), A Comparison of Seasonal Winds With Currents on the Continental Slope of
35 the Catalan Sea (Northwestern Mediterranean), *J. Geophys. Res.*, 95(C2), 1537–1545,

- 1 doi:10.1029/JC095iC02p01537.
- 2 Grifoll, M., A. L. Aretxabaleta, J. L. Pelegrí, M. Espino, J. C. Warner, and A. Sánchez-Arcilla
3 (2013), Seasonal circulation over the Catalan inner-shelf (northwest Mediterranean Sea),
4 *J. Geophys. Res. Ocean.*, *118*(10), 5844–5857, doi:10.1002/jgrc.20403.
- 5 Hasselmann, K., 1974. On the spectral dissipation of ocean waves due to white-capping.
6 *Boundary-Layer Meteorol.* *6*, 107–127.
- 7 Horwitz, R., and S. J. Lentz (2014), Inner-Shelf Response to Cross-Shelf Wind Stress: The
8 Importance of the Cross-Shelf Density Gradient in an Idealized Numerical Model and
9 Field Observations, *J. Phys. Oceanogr.*, *44*(1), 86–103, doi:10.1175/JPO-D-13-075.1.
- 10 Jacob, R., J. Larson and E. Ong (2005) M x N communication and parallel interpolation in
11 CCSM using the Model Coupling Toolkit. Preprints, Mathematics and Computer Science
12 Division, Argonne National Laboratory, Argonne, IL.
- 13 Jansà, A. (1985). The “Mistral-Tramuntana” shear line. A satellite observation. Scientific
14 results of the alpine experiment (ALPEX). Grap publications series, 27, Volume II, 577-
15 591.
- 16 Janssen, P. (1989), Wave-induced stress and the drag of air flow over sea waves, *J. Phys.*
17 *Oceanogr.*, *19*, 745–754.
- 18 Janssen, P.A.E.M., (1991). Consequences of the effect of surface gravity waves on the mean
19 air flow. In: International Union of Theory and Applied Mechanics (IUTAM), Sydney,
20 Australia, 193–198.
- 21 Janssen, P., and P. Viterbo (1996), Ocean waves and the atmospheric climate, *J. Clim.*, *9*,
22 1269–1287.
- 23 Jiang, H., J. T. Farrar, R. C. Beardsley, R. Chen, and C. Chen (2009), Zonal surface wind jets
24 across the Red Sea due to mountain gap forcing along both sides of the Red Sea,
25 *Geophys. Res. Lett.*, *36*(19), L19605, doi:10.1029/2009GL040008.
- 26 Jones, P. (1999), First- and second-order conservative remapping schemes for grids in
27 spherical coordinates, *Mon. Weather Rev.*, (3), 2204–2210.
- 28 Jordà, G. (2005), Towards data assimilation in the Catalan continental shelf. From data
29 analysis to optimization methods, PhD thesis, Univ. Politècnica de Catalunya, Barcelona,
30 Spain.
- 31 Klaić, Z. B., Z. Pasarić, G. Beg Paklar, and P. Oddo (2011), Coastal sea responses to
32 atmospheric forcings at two different resolutions, *Ocean Sci.*, *7*(4), 521–532,
33 doi:10.5194/os-7-521-2011.
- 34 Lionello, P., P. Malaguzzi, and A. Buzzi (1998), Coupling between the Atmospheric
35 Circulation and the Ocean Wave Field: an idealized case., (1), 161–177.

- 1 Martín-Vide, J. and J. Olcina, J. (2001). Climas y Tiempos de España, Alianza editorial,
2 Madrid, Spain. 264 pag. In spanish.
- 3 Mestres, M., J. P. Sierra, A. Sánchez-arcilla, J. González, Del Río, T. Wolf, and A. Rodríguez
4 (2003), Modelling of the Ebro River plume . Validation with field observations , *67*(4),
5 379–391.
- 6 Nelson, J. and R. He (2012), Effect of the Gulf stream on winter extratropical cyclone
7 outbreaks. *Atmos Sci Lett* 13:311–316. doi:10.1002/asl.400
- 8 Nunalee, C., and S. Basu (2014), Mesoscale modeling of coastal low level jets: implications
9 for offshore wind resource estimation, *Wind Energy*, doi:10.1002/we.
- 10 Oddo, P., A. Bonaduce, N. Pinardi, and A. Guarnieri (2014), Sensitivity of the Mediterranean
11 sea level to atmospheric pressure and free surface elevation numerical formulation in
12 NEMO, *Geosci. Model Dev.*, 7(6), 3001–3015, doi:10.5194/gmd-7-3001-2014.
- 13 Olabarrieta, M., J. C. Warner, B. Armstrong, J. B. Zambon, and R. He (2012), Ocean–
14 atmosphere dynamics during Hurricane Ida and Nor’Ida: An application of the coupled
15 ocean–atmosphere–wave–sediment transport (COAWST) modeling system, *Ocean
16 Model.*, 43-44, 112–137, doi:10.1016/j.ocemod.2011.12.008.
- 17 Oost, W. A., G. J. Komen, C. M. J. Jacobs, and C. van Oort (2002), New evidence for a
18 relation between wind stress and wave age from measurements during ASGAMAGE,
19 *Bound. Layer Meteorology*, 103, 409–438.
- 20 Palanques, A., P. Puig, and J. Guillén (2002), Near-bottom suspended sediment fluxes on the
21 microtidal low-energy Ebro continental shelf (NW Mediterranean), *Cont. Shelf*, 22,
22 285–303.
- 23 Pallares, E., Sánchez-Arcilla, A. and M. Espino (2016), Wave energy balance in wave models
24 (SWAN) for semi-enclosed domains—Application to Catalan coast, *Cont. Shelf*, 87, 41-
25 53.
- 26 Redondo, J. M., A. Matulka, A. Platonov, E. Sekula, and P. Fraunie (2013), Eddy
27 measurements, coastal turbulence and statistics in the gulf of Lions, *Ocean Sci. Discuss.*,
28 10(1), 55–81, doi:10.5194/osd-10-55-2013.
- 29 Renault, L., J. Chiggiato, J. C. Warner, M. Gomez, G. Vizoso, and J. Tintoré (2012), Coupled
30 atmosphere-ocean-wave simulations of a storm event over the Gulf of Lion and Balearic
31 Sea, *J. Geophys. Res. Ocean.*, 117(C9), n/a–n/a, doi:10.1029/2012JC007924.
- 32 Ricchi A., M. M. Miglietta, P. P. Falco, A. Bergamasco, A. Benetazzo, D. Bonaldo, M. Sclavo,
33 and S. Carniel (2016), On the use of a coupled ocean-atmosphere-wave model during an
34 extreme Cold Air Outbreak over the Adriatic Sea, *Atmospheric Research* 172–173, 48–
35 65.
- 36 Riosalido, L., Vazquez, A., A. Gordo, A. and A., Jansà (1985). “Cierzo”: northwesterly wind

- 1 along the Ebro Valley as a meso-scale effect induced on the lee of the Pyrennes mountain
2 range; a case study during alpeX special observing period. Scientific results of the alpine
3 experiment (ALPEX). Grap publications series, 27, Volume II, 565-575.
- 4 Salat, J. et al. (2002), Seasonal changes of water mass structure and shelf slope exchanges at
5 the Ebro Shelf (NW Mediterranean), *Cont. Shelf Res.*, 22, 327–348.
- 6 Sánchez-Arcilla, A., D. González-Marco, and R. Bolaños (2008), A review of wave climate
7 and prediction along the Spanish Mediterranean coast, *Nat. Hazards Earth Syst. Sci.*,
8 8(6), 1217–1228, doi:10.5194/nhess-8-1217-2008.
- 9 Schaeffer, A., P. Garreau, A. Molcard, P. Fraunié, and Y. Seity (2011), Influence of high-
10 resolution wind forcing on hydrodynamic modeling of the Gulf of Lions, *Ocean Dyn.*,
11 61(11), 1823–1844, doi:10.1007/s10236-011-0442-3.
- 12 Shimada, T., and H. Kawamura (2006), Wind-wave development under alternating wind jets
13 and wakes induced by orographic effects, *Geophys. Res. Lett.*, 33(2), L02602,
14 doi:10.1029/2005GL025241.
- 15 Skamarock, W.C., Klemp, J.B., Dudhia, J., Gill, D.O., Barker, D.M., Wang, W., Powers, J.G.,
16 (2005). A Description of the Advanced Research WRF, Version 2, NCAR Technical
17 Note, NCAR/TN-468+STR.
- 18 Spanish Ministry of Energy (2014), Wind Atlas of Spain; www.mineturb.gov.es
- 19 Taylor, P., and M. Yelland (2001), The dependence of sea surface roughness on the height and
20 steepness of the waves, *J. Phys. Oceanogr.*, (1996), 572–590.
- 21 Tonani M., A. Teruzzi, G. Korres, N. Pinaridi, A. Crise, M. Adani, P. Oddo, S. Dobricic, C.
22 Fratianni, M. Drudi, S. Salon, A. Grandi, G. Girardi, V. Lyubartsev and S. Marino, 2014.
23 The Mediterranean Monitoring and Forecasting Centre, a component of the MyOcean
24 system. Proceedings of the Sixth International Conference on EuroGOOS 4-6 October
25 2011, Sopot, Poland. Edited by H. Dahlin, N.C. Fleming and S. E. Petersson. First
26 published 2014. Eurogoos Publication no. 30. ISBN 978-91-974828-9-9.
- 27 Umlauf, L., and H. Burchard (2003), A generic length-scale equation for geophysical, *J. Mar.*
28 *Res.*, 61(2), 235–265, doi:10.1357/002224003322005087.
- 29 Warner, J. C., B. Armstrong, R. He, and J. B. Zambon (2010), Development of a Coupled
30 Ocean–Atmosphere–Wave–Sediment Transport (COAWST) Modeling System, *Ocean*
31 *Model.*, 35(3), 230–244, doi:10.1016/j.ocemod.2010.07.010.
- 32 Warner, J. C., C. R., Sherwood, R. P. Signell, C.K., Harris and H.G. Arango (2008).
33 Development of a three-dimensional, regional, coupled wave, current, and sediment-
34 transport model, *Computers & Geosciences*, 34, 1284-1306,
35 doi:10.1016/j.cageo.2008.02.012
- 36 WAMDI group,1988.TheWAMmodel – a third generation ocean wave prediction model.

1 *J.Phys.Oceanogr.*18,1775–1810.

2 Zambon, J. B., R. He, and J. C. Warner (2014), Investigation of hurricane Ivan using the
3 coupled ocean–atmosphere–wave–sediment transport (COAWST) model, *Ocean Dyn.*,
4 64(11), 1535–1554, doi:10.1007/s10236-014-0777-7.

5 Zhai, P., and A. Bower (2013), The response of the Red Sea to a strong wind jet near the
6 Tokar Gap in summer, *J. Geophys. Res. Ocean.*, 118(1), 421–434,
7 doi:10.1029/2012JC008444.

8

1 Table 1. Resolution (in km) of the different domains/meshes used in the nested system as a
 2 function of each numerical model and regional scale covered. In parentheses the mesh name
 3 in Fig. 1 is shown.

Model	NW Mediterranean	Catalan—Balearic Sea	Catalan coast	Ebro delta
WRF	27 (M1)	9 (M2)	3 (M3)	1 (M4)
SWAN	9 (O1)	3 (O2)	1 (O3)	¼ (O4)
ROMS	-	-	1 (O3)	¼ (O4)

4

1 Table 2. Statistics for the comparison between buoy measurements and model outputs. W is
 2 the wind intensity (in $\text{m}\cdot\text{s}^{-1}$), Hs is the significant waves height (in m), Tm₀₁ is the mean wave
 3 period (in s) and U are the depth-averaged along-shelf currents (in $\text{cm}\cdot\text{s}^{-1}$; positive north-
 4 eastward). The statistical parameters are the root mean square error (RMSE), the bias and the
 5 correlation coefficient (R).

	Observed		RMSE	Bias	R
	Mean	Standard deviation			
W	6.59	4.52	2.70	0.68	0.79
Hs	0.62	0.42	0.29	0.09	0.76
Tm ₀₁	3.48	0.92	3.57	1.14	0.57
U	-4.60	3.90	3.07	2.14	0.82

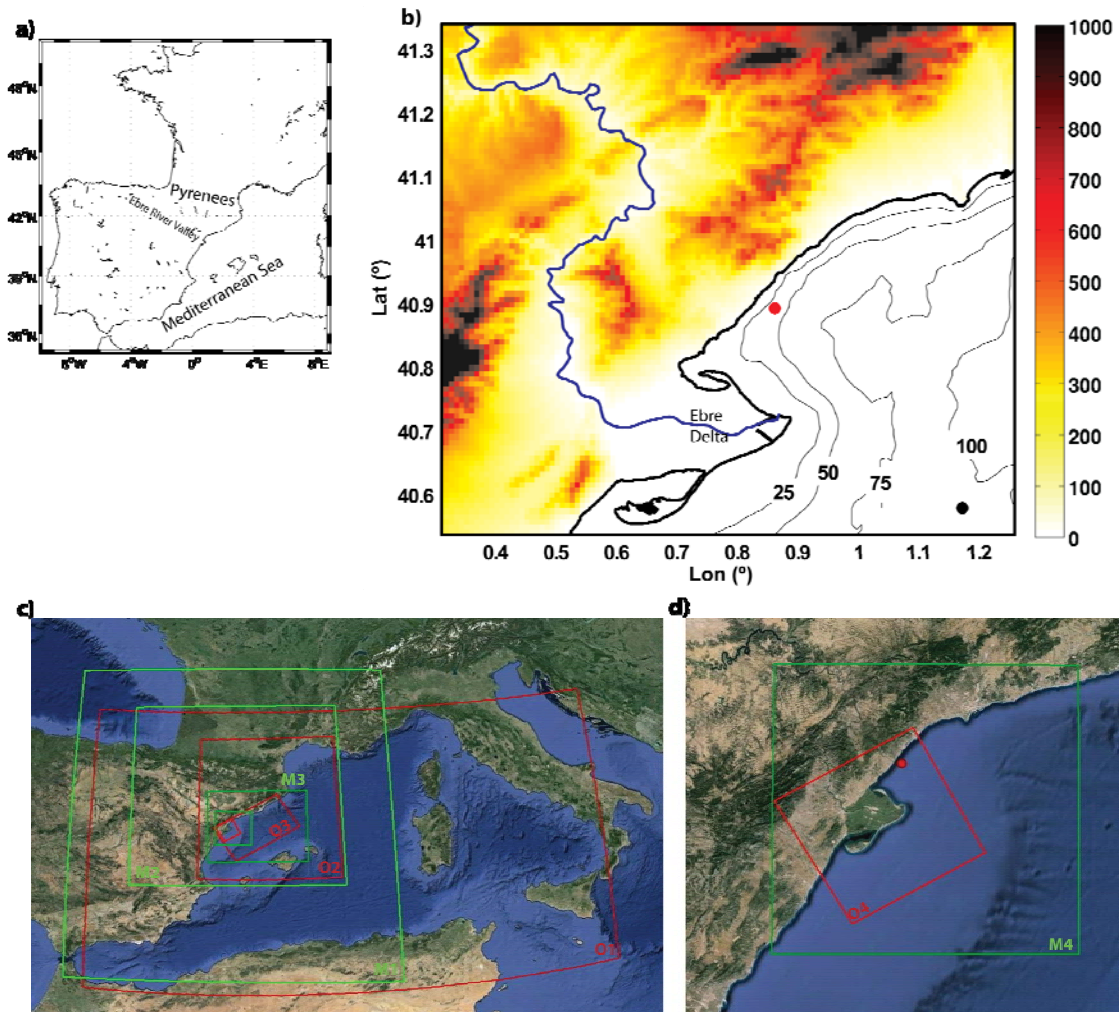
6

1 Table 3. Statistics for the comparison between buoy measurements and model outputs. W is
 2 the wind intensity (in $\text{m}\cdot\text{s}^{-1}$); Hs is the significant waves height (in m). Statistics are only for
 3 the wind jet event (i.e. from 20 to 23 of May 2012).

		Mean	Standard deviation	RMSE	R
		obs/mod	obs/mod		
CHK	W	10.93/11.48	5.65/5.19	4.75	0.62
	Hs	0.74/0.73	0.27/0.32	0.25	0.61
T-Y	W	10.93/11.51	5.65/5.24	4.83	0.61
	Hs	0.74/0.72	0.27/0.31	0.26	0.61
DRE	W	10.93/11.46	5.65/5.24	4.79	0.61
	Hs	0.74/0.72	0.27/0.31	0.26	0.62
OOST	W	10.93/11.47	5.65/5.22	4.85	0.60
	Hs	0.74/0.72	0.27/0.31	0.26	0.61

4

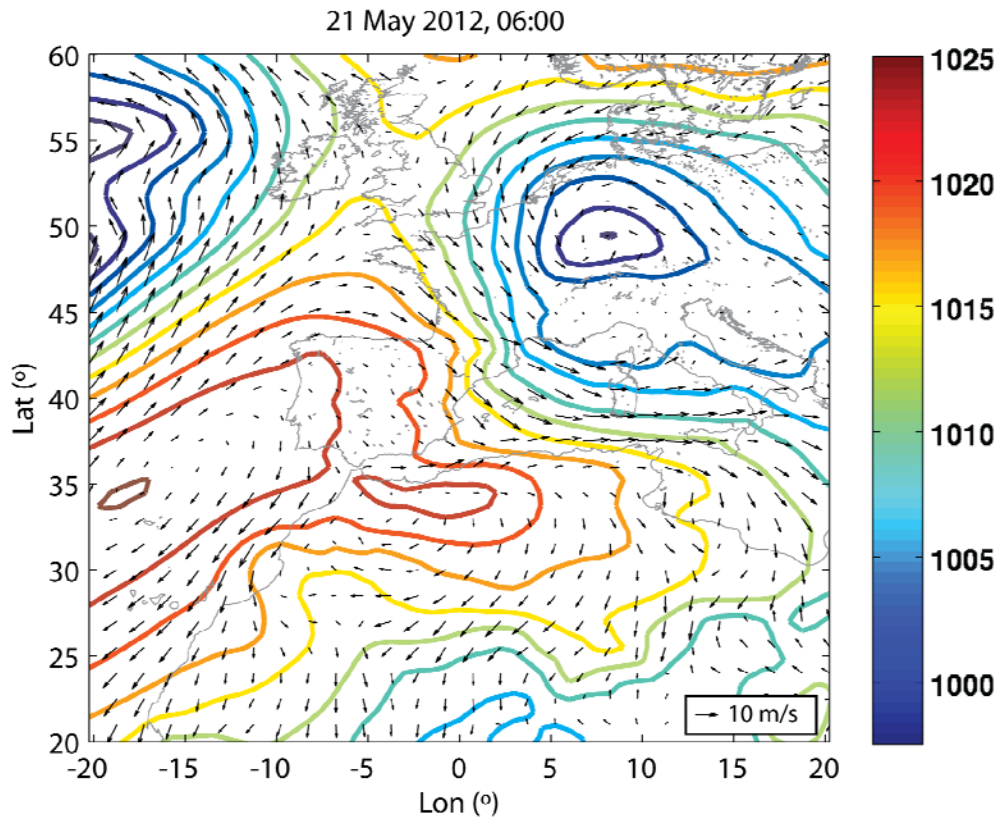
1



2

3 Figure 1. Localization map (a) and orography (coloured map) and bathymetry of the study
4 area (b). The bathymetry lines are shown every 25m. The geographical position where the
5 observational buoy was moored is shown with a red circle. The control point used in the
6 analysis is shown with a black circle. (c, d) Geographical domains for the meteorological
7 model (in green) and the wave and the water circulation model (in red).The mesh notation is
8 also shown (its resolution is detailed in Table 1).

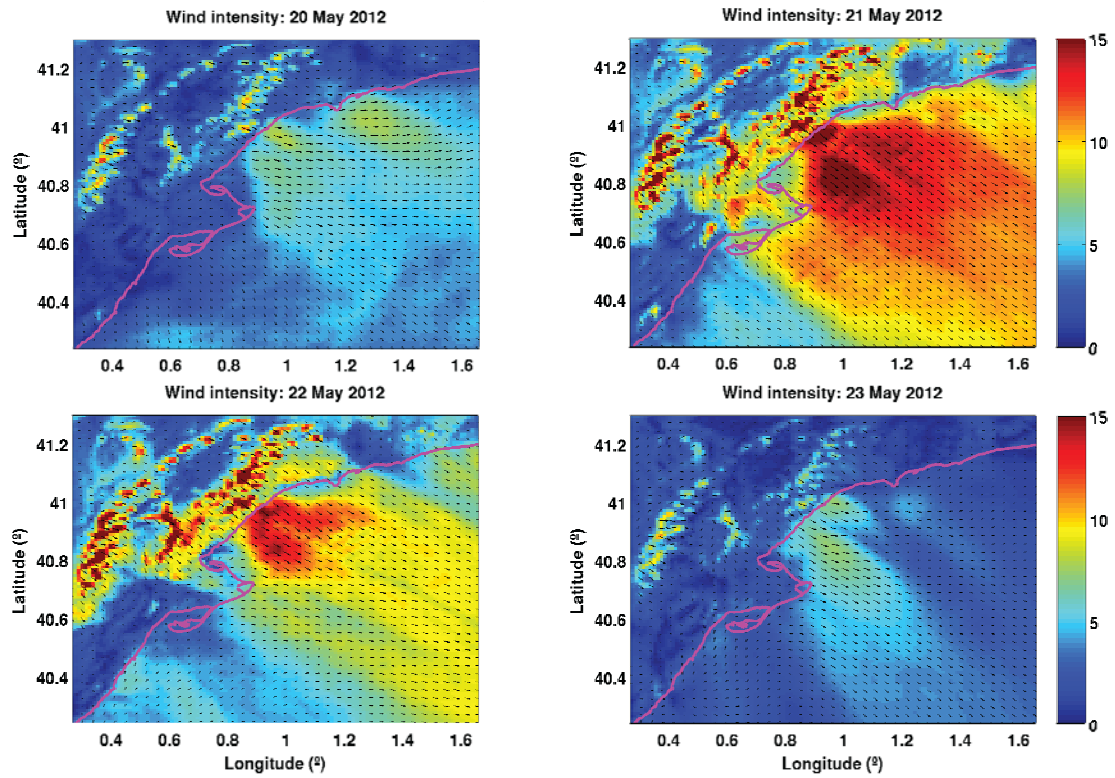
1



2

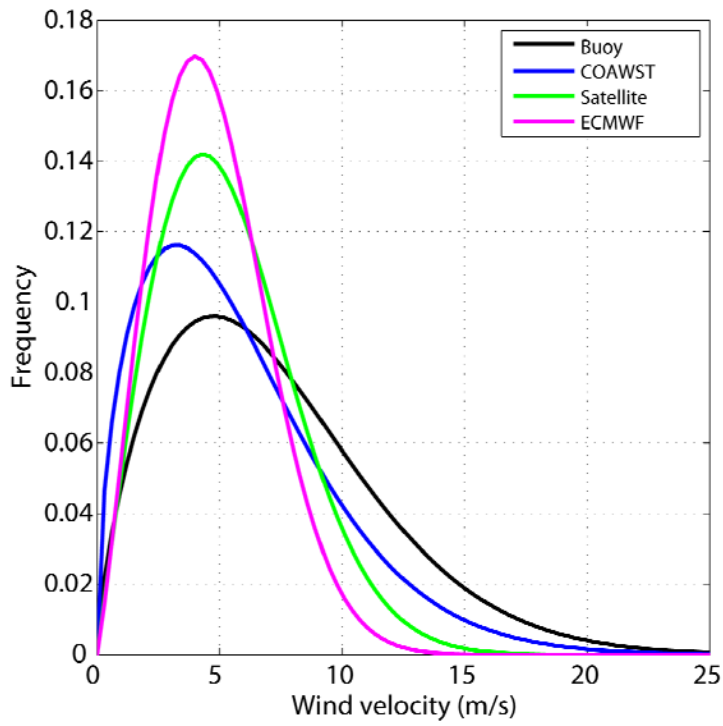
3 Figure 2. Regional chart of the mean sea level pressure (hPa) during the 21st of May at 06:00
4 UTC (representative of the synoptic situation during the selected cross-shelf wind event).
5 Data source: ERA-Interim global reanalysis from ECMWF. Arrows represent the wind field.

6



1

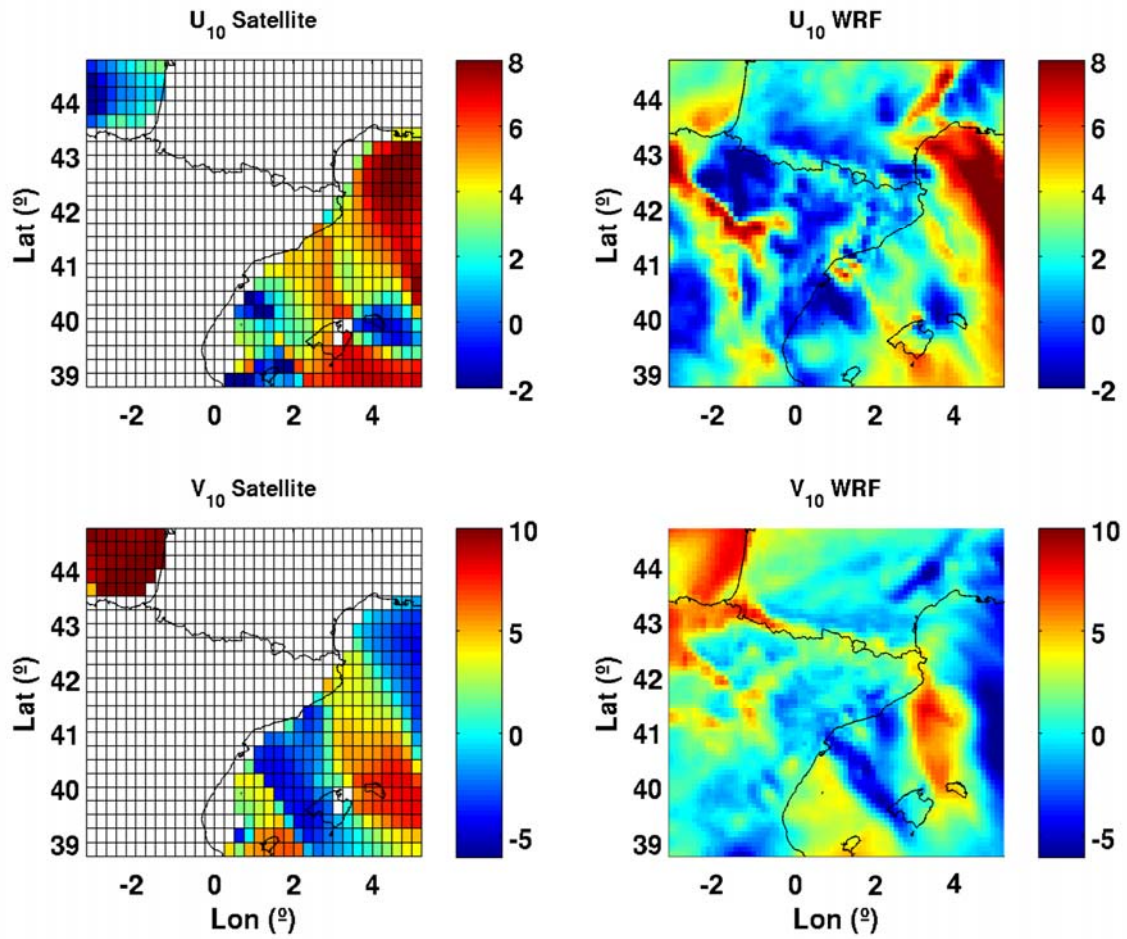
2 Figure 3. Sequence of the wind jet intensity on four days for a wind jet event in the domain of
 3 the Catalan coast. The quiver is shown each three points. Results obtained for COAWST at
 4 mesh M3 are plotted.



1

2 Figure 4. Weibull distribution adjustment for the wind velocities regarding the duration for
3 the entire 12 months analysed.

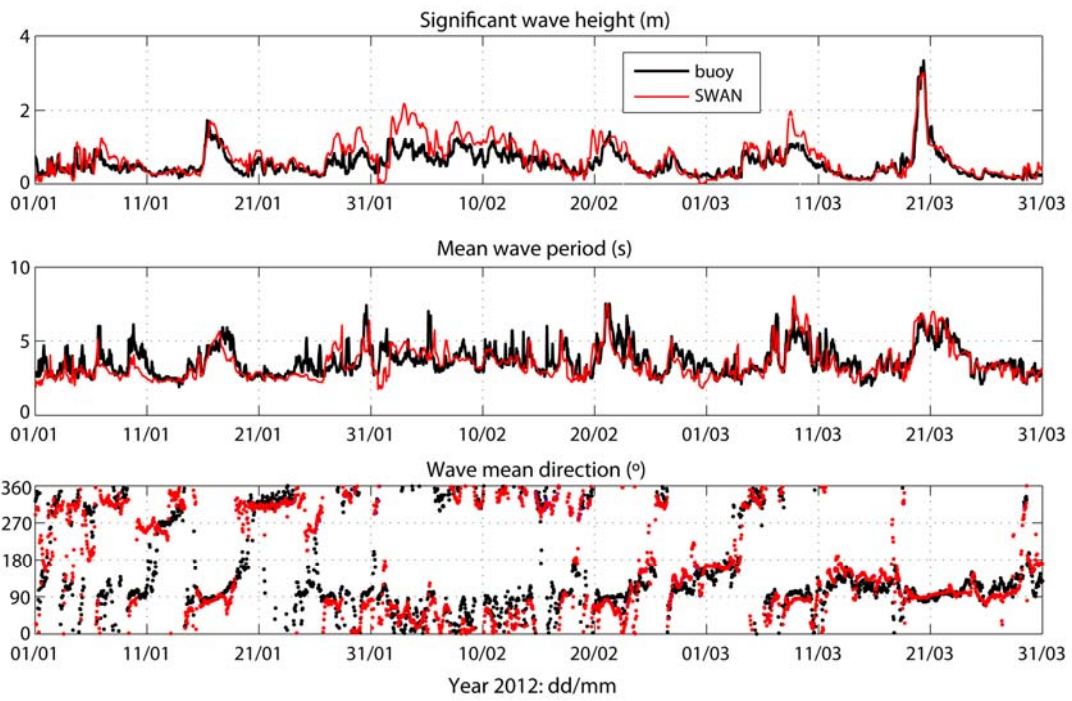
1
2



3

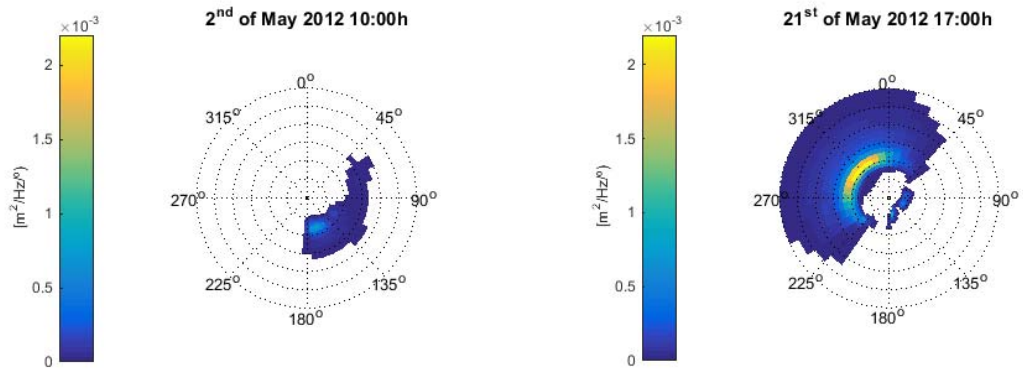
4 Figure 5. Wind components (top: east—west top; bottom: north—south)
5 gridded product for the study area (top) and from the results of the meteorological model
6 (mesh M1). The figure corresponds to 01/01/2012 at 12:00 UTC.

1



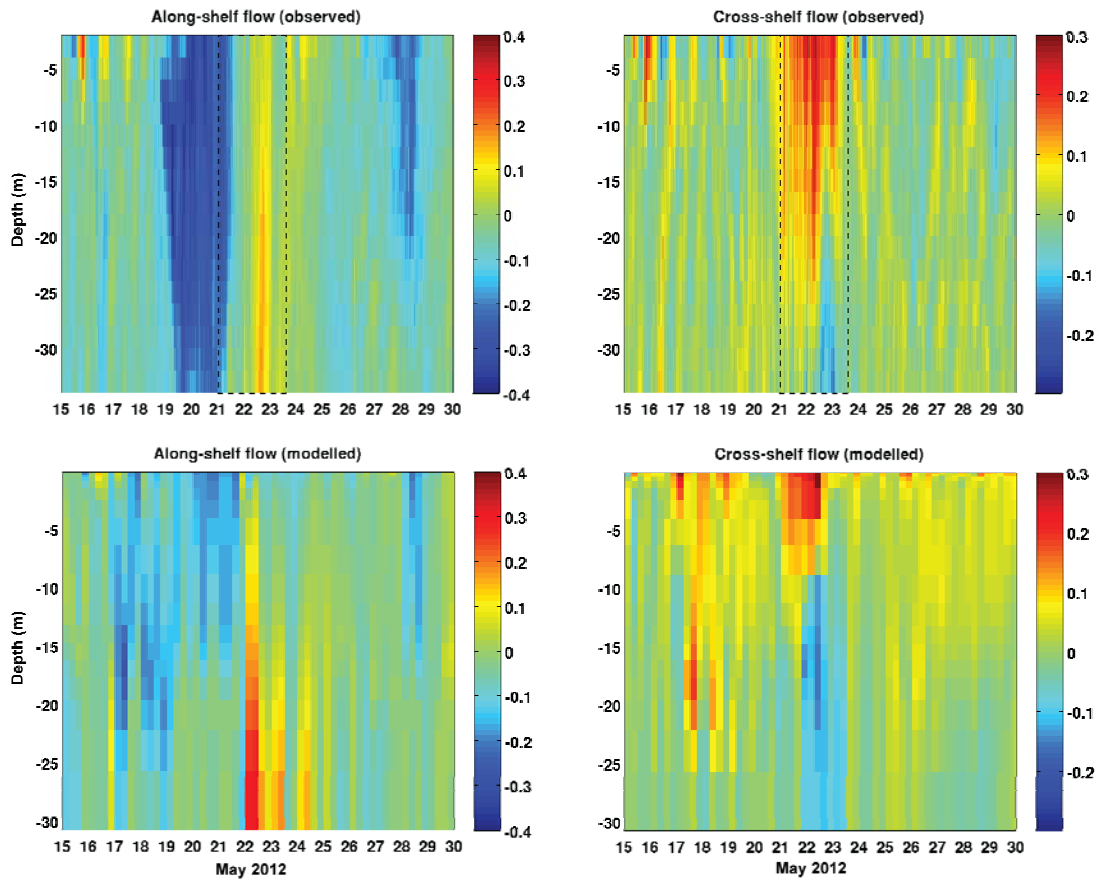
2

3 Figure 6. Time series of the significant wave height (m), the mean wave period T_{m01} (s) and
4 the mean wave direction for the first trimester of 2012. In black the buoy measurement is
5 represented and in red the SWAN numerical results.



1

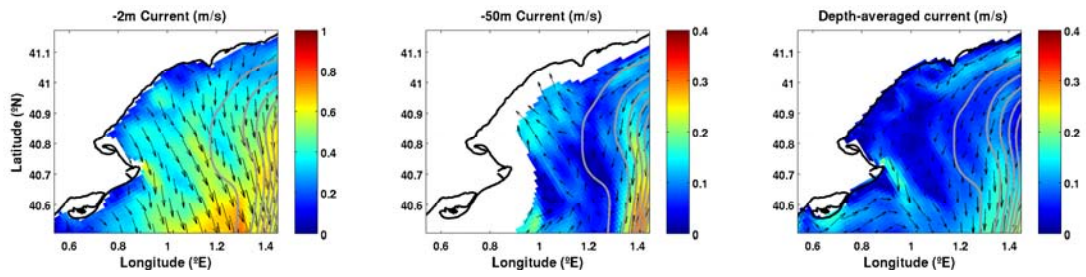
2 Figure 7. Numerical wave spectra for two different instants at the observational point: without
 3 wind jet event (left; 2nd March 2012) and during wind jet event (right; 21st March 2012).



1

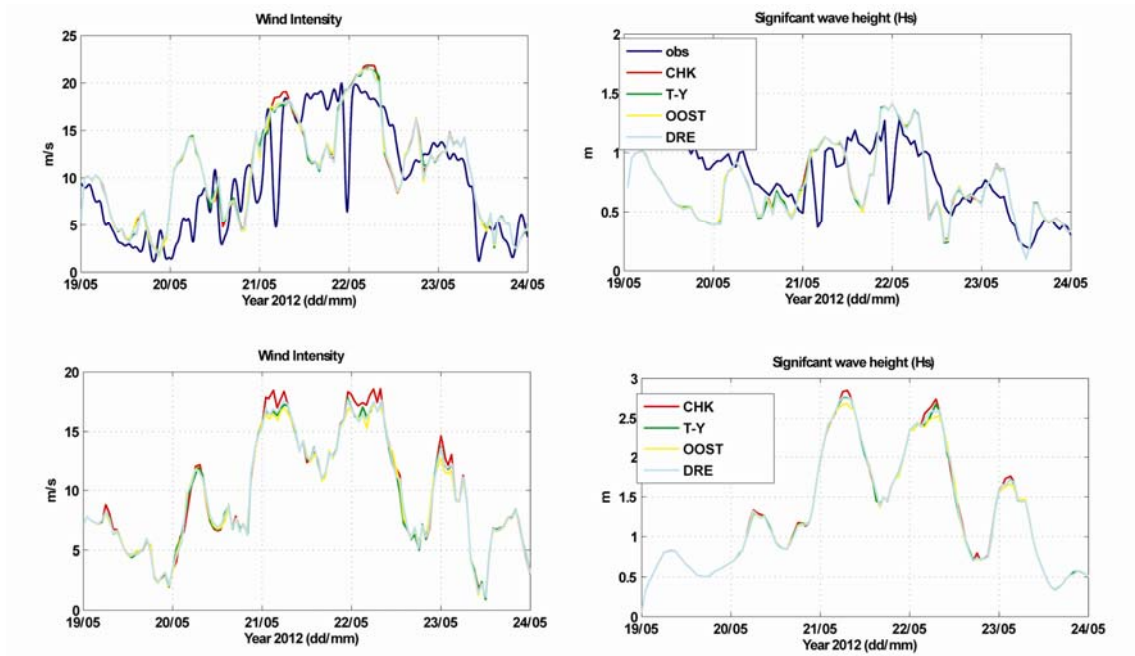
2 Figure 8. Along-shelf (left) and cross-shelf (right) velocity observed (top) and modelled
 3 (bottom) during May 2012 (in m/s). Positive means north-eastward and offshore. The wind jet
 4 period is marked as a dashed square in the observed values. Note the different velocity ranges
 5 between cross-shelf and along-shelf plots.

1



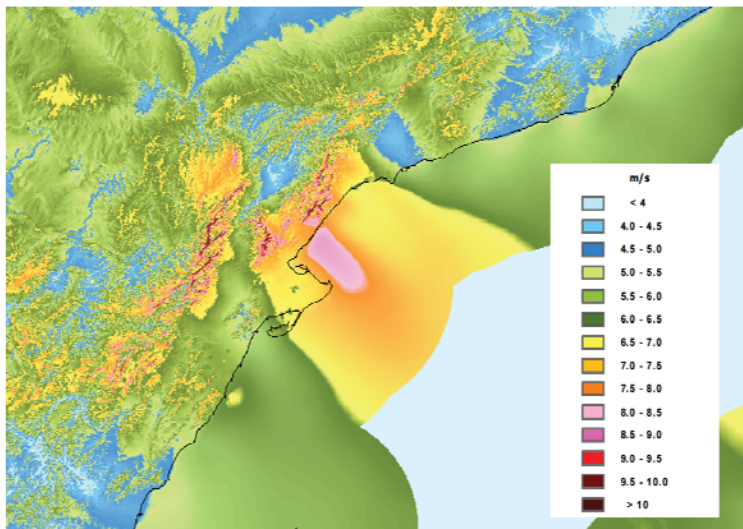
2

3 Figure 9. Modelled circulation at -2m (left), -50m (centre) and depth-averaged circulation
4 (right) during the peak of the wind jet event (i.e. 21st of May 2012, 06:00 UTC). The quiver is
5 shown each four computational points. Grey lines are shown each 100 isobaths. Note
6 differences in the velocity ranges among the sub-plots.



1

2 Figure 10. Wind intensity (left) and significant wave height (right) for the wind jet energetic
 3 event for the observational (top) and control (bottom) points.



1

2 Figure 11. Wind atlas annual mean wind speed at 30m height from a reanalysis product
3 (source: Spanish Ministry of Energy, 2014).

4